AIAA JOURNAL
Vol. 38, No. 12, December 2000

Three-Dimensional Corotational Framework for Elasto–Plastic Analysis of Multilayered Composite Shells

Arif Masud* and Choon L. Tham†
University of Illinois at Chicago, Chicago, Illinois 60607-7023

A continuum based layerwise shear-deformable finite element formulation is presented for elasto–plastic analysis of layered composites shells. The proposed formulation is cast in a corotational configuration for finite deformation analysis. The elasto–plastic constitutive equations that are based on rate-independent deviatoric plasticity are also written in the corotational kinematic framework. Issues of covariance and spatial invariance are addressed, and an appropriate stress updating strategy is proposed. Numerical examples are presented to demonstrate the range of applicability of the proposed framework for bending-dominated response of elasto–plastic layered composite shells.

Nomenclature

$\boldsymbol{b}$	=	body force vector
$\boldsymbol{C}^e$	=	fourth-order elastic modulus tensor
$\boldsymbol{c}^{(i)}_{n+1}$	=	tangent modului consistent with the radial return algorithm
$\boldsymbol{d}^p$	=	plastic strain rate tensor
$\boldsymbol{e}$	=	deviatoric strain tensor
$\bar{e}^p$	=	equivalent plastic strain
$\bar{\boldsymbol{F}}_{n+1}$	=	incremental deformation gradient
$\boldsymbol{F}_t(\boldsymbol{X})$	=	deformation gradient
$f(\boldsymbol{\sigma}, \boldsymbol{q})$	=	von Mises pressure-insensitive yield condition
$\mathcal{H}_\alpha(\bar{e}^p)$	=	hardening rule for back stress
$\boldsymbol{I}$	=	identity matrix
J_2	=	second invariant
K	=	bulk modulus
n_{sd}	=	number of spatial dimensions
$\hat{\boldsymbol{n}}$	=	unit normal to the yield surface
$\boldsymbol{q}$	=	$\{\boldsymbol{\alpha}, \bar{e}^p\}$ set of internal variables
R_{n+1}	=	radius of the yield surface
$\tilde{\boldsymbol{R}}^{(i)}_{n+1}$	=	local rotational matrix in coordinate system associated with $\tilde{\Omega}^{(i)}_{n+1}$
$\mathcal{S}$	=	space of admissible configurations
$\boldsymbol{s}$	=	deviatoric stress tensor
$\boldsymbol{s}^{\text{trial}}_{n+1}$	=	trial elastic stress
$\boldsymbol{t}$	=	traction vector
$\bar{\boldsymbol{u}}^{(i)}_{n+1}$	=	incremental displacement of the spatial domain from Ω_n to $\Omega^{(i)}_{n+1}$
$\tilde{\boldsymbol{u}}^{(i)}_{n+1}$	=	incremental displacement from $\tilde{\Omega}_n$ to current rotated configuration $\tilde{\Omega}^{(i)}_{n+1}$
$\mathcal{V}$	=	space of admissible variations
$\boldsymbol{X} \in \Omega_0$	=	material points
$\boldsymbol{x} \in \Omega_t$	=	spatial points
$\tilde{\boldsymbol{x}}$	=	points in the corotational configuration in domain $\tilde{\Omega}_t$
$\boldsymbol{\alpha}$	=	back stress
Γ_{g_0}	=	portion of boundary with prescribed essential boundary conditions
Γ_{h_0}	=	portion of boundary with prescribed natural boundary conditions
γ	=	consistency parameter
$\Delta\boldsymbol{d}^{\text{def}(i)}_{n+1}$	=	deformational part of the displacements
$\Delta\tilde{\boldsymbol{d}}^{\text{def}(i)}_{n+1}$	=	deformational part of displacements in the local corotational system
$\Delta\boldsymbol{d}^{\text{rig}(i)}_{n+1}$	=	rigid-body translations
$\boldsymbol{\eta}_0$	=	admissible virtual displacement field
$\kappa(\bar{e}^p)$	=	hardening rule for the radius of the yield surface
μ	=	shear modulus
$\boldsymbol{\sigma}$	=	Cauchy stress
$\boldsymbol{\sigma}^{\nabla\text{GN}}$	=	Green–Naghdi stress rate
$\varphi(\boldsymbol{X}, t)$	=	current placement of the body
$\bar{\varphi}(\boldsymbol{x}, t)$	=	incremental mapping from Ω_n to Ω_{n+1}
$\Omega_0 \subset R^{n_{\text{sd}}}$	=	reference placement of a continuum body
$(\cdot)^{\text{trial}}_{n+1}$	=	trial elastic quantity
$\|\cdot\|$	=	norm associated with the inner product of the indicated quantity

I. Introduction

LAMINATED composites continue to be of great interest for aerospace and mechanical engineering applications. These engineered materials possess superior properties as compared to their constituent parent materials. With the advances in materials science and developments in better fabrication processes, modern laminated composites are now being used in critical engineering applications. Some applications involve large elastic deformations, for example, helicoptor rotor blades, whereas there are others that require a complete analysis of the elasto–plastic response of the constituent materials. Various approaches have been proposed to model nonlinear response in these materials.[1,2] For recent reviews on composite elements see Refs. 3 and 4.

This paper presents a continuum-based layerwise shear deformable formulation to model large deformation elasto–plastic response in multilayered composite shells. The proposed formulation is most suited for the class of layered composites wherein the thickness of the constituent layers is comparable to the overall thickness of the composite laminate. Even a small deformation in this class of composites results in warping (in-plane distortion) of the deformed normal.[5] The present work is an extension of earlier efforts,[6,7] wherein we addressed geometric nonlinearity in multilayered composites. In the present work, we endeavor to extend this framework to incorporate material nonlinearity as well. The elasto–plastic constitutive model is based on associative J_2 plasticity.[8–10] The model is then cast in a corotational framework to simulate large deformation response, wherein displacements and rotations are assumed finite and the strains are assumed to lie in the small to moderate range. Technical issues related to the use of small to moderate strain nonlinear constitutive equations for large deformation analysis via casting these equations in the corotational kinematic framework are addressed. Note that strains when measured in the corotational frame, although being small, are not exactly the strains of the small deformation theory. Accordingly, the issue of material

Received 27 August 1999; revision received 20 November 1999; accepted for publication 30 April 2000.

*Assistant Professor of Mechanics and Materials, Department of Civil and Materials Engineering (MC 246); Amasud@uic.edu.

†Graduate Research Assistant, Department of Civil and Materials Engineering.

frame indifference or objectivity of stress, because it is being calculated based on the strains measured in the corotational frame, needs careful attention.[11–14]

We start with a discussion of finite deformation kinematics within the context of the corotational framework. The small strain elasto–plastic constitutive model that is based on rate indepenedent deviatoric plasticity is cast in this corotational frame. We then present the radial return algorithm for numerical integration of constitutive equations. The variational form of the problem together with a discussion of the consistent tangent operator is given next. Thereafter, we present some numerical results to show the range of application of the proposed formulation and close with some concluding remarks.

II. Kinematics in the Corotational Configuration

We discuss finite deformation kinematics within the context of the corotational framework for nonlinear analysis. Figure 1 is a schematic diagram of the referential, spatial, and corotational domains. Let $\Omega_0 \subset R^{n_{sd}}$ be the reference placement of a continuum body with particles labeled as $\boldsymbol{X} \in \Omega_0$, and $n_{sd} \geq 2$ denotes the number of spatial dimensions. We refer to $\varphi(\boldsymbol{X}, t)$ as the current placement of the body with points designated $\boldsymbol{x} \in \Omega_t$. The deformation gradient $\boldsymbol{F}$ is denoted as $\boldsymbol{F}_t(\boldsymbol{X}) = D\varphi_t(\boldsymbol{X})$. Incremental mapping from Ω_n to Ω_{n+1} is indicated as $\bar{\varphi}(\boldsymbol{x}, t) = \bar{\varphi}[\varphi_t(\boldsymbol{X}), t]$. Consequently, the incremental deformation gradient $\bar{\boldsymbol{F}}_{n+1}$ between Ω_n and Ω_{n+1} is defined as

$$\bar{\boldsymbol{F}}_{n+1} = \frac{\partial \boldsymbol{x}_{n+1}}{\partial \boldsymbol{x}_n} = \boldsymbol{1} + \nabla \bar{\boldsymbol{u}}^{(i)}_{n+1} \tag{1}$$

To develop the corotational procedure, we introduce another mapping $\tilde{\varphi}(\boldsymbol{x}, t)$ that corresponds to the rotation of the body from Ω_n to $\tilde{\Omega}_n$ and yields a description of the body in the rotated frame such that

$$\tilde{\boldsymbol{x}} = \tilde{\varphi}(\boldsymbol{x}, t) = \tilde{\varphi}[\varphi_t(\boldsymbol{X}), t] \tag{2}$$

From Eq. (2), the deformation gradient from Ω_n to $\tilde{\Omega}_n$ is defined as

$$\tilde{\boldsymbol{F}}_t(\boldsymbol{x}) = D\tilde{\varphi}_t(\boldsymbol{x}) = \frac{\partial \tilde{\varphi}_t(\boldsymbol{x})}{\partial \boldsymbol{x}} \tag{3}$$

Equation (3) gives rise to the orthonormal corotation tensor indicated as $\boldsymbol{R}$. However, in the computational setting $\boldsymbol{R}$ is usually obtained via a local corotational coordinate system associated with each element in the discretized domain that undergoes rigid-body rotations and translations with the element. Furthermore, incremental mapping from $\tilde{\Omega}_n$ to $\tilde{\Omega}_{n+1}$ is indicated as $\tilde{\varphi}(\tilde{\boldsymbol{x}}, t) = \tilde{\varphi}(\tilde{\varphi}_t(\boldsymbol{x}), t)$. Accordingly, the incremental deformation gradient is

$$\tilde{\boldsymbol{F}}_{n+1} = \frac{\partial \tilde{\varphi}(\tilde{\boldsymbol{x}}, t)}{\partial \tilde{\boldsymbol{x}}_n} = \boldsymbol{1} + \nabla \tilde{\boldsymbol{u}}^{(i)}_{n+1}$$

In the corotational procedure we consider that an arbitrary motion of a general continuous medium can be decomposed into a rigid-body motion, superposed by a pure relative deformation. If the incremental motion is sufficiently small, the pure deformation part of the displacement field that is obtained by subtracting rigid-body motion from the total displacement is small. Consequently, the magnitude of strains when measured in the rotated frame is of the order of infinitesimal strains. In the spatially discretized domain, this decomposition can be accomplished by defining a local corotational coordinate frame, for example, for each element, that translates and rotates with the element, but does not deform with the element. The pure deformation part of the displacement field in an element, when measured with respect to this local convected frame, is small as compared to the element dimensions. Consequently, discrete gradients of the pure deformational displacement field measured in the local corotated frame are of the order of small strains (e.g., see Belytschko and Hsieh[15]). This is the key idea that is employed to simplify the updated Lagrangian formulation to the corotational formulation.

With the objective of presenting elasto–plasticity in the corotational framework, we first discuss the issue of decomposition of the total displacement into rigid-body motion and pure relative deformation. We assume that we know the reference configuration $\tilde{\Omega}_n$, which is the converged state in the corotational frame at the end of the previous step. Assume that the local corotational coordinate system associated with a typical element rotates from $\tilde{\boldsymbol{R}}_n$ in $\tilde{\Omega}_n$ to $\tilde{\boldsymbol{R}}^{(i)}_{n+1}$ in the latest obtained configuration $\tilde{\Omega}^{(i)}_{n+1}$. The translational displacements induced by the rigid-body rotation of the element can be expressed in the global coordinate system as

$$\Delta \boldsymbol{d}^{\mathrm{rig}(i)}_{n+1} = \left[\tilde{\boldsymbol{R}}^{(i)}_{n+1}\tilde{\boldsymbol{R}}^{T}_{n} - \boldsymbol{I}\right]\boldsymbol{x}_n \tag{4}$$

where $\boldsymbol{x}_n$ indicates the global nodal-coordinate vector in configuration Ω_n. Subtracting $\Delta \boldsymbol{d}^{\mathrm{rig}(i)}_{n+1}$ from the displacement increments $\Delta \boldsymbol{d}^{(i)}_{n+1}$ gives the deformational part of the displacements $\Delta \boldsymbol{d}^{\mathrm{def}(i)}_{n+1}$. Transforming it to the current local corotational coordinate system, we obtain the pure deformational part of the displacements (in the local corotational system) as follows:

$$\Delta \tilde{\boldsymbol{d}}^{\mathrm{def}(i)}_{n+1} = \tilde{\boldsymbol{R}}^{T(i)}_{n+1}\left(\boldsymbol{x}_n + \Delta \boldsymbol{d}^{(i)}_{n+1}\right) - \tilde{\boldsymbol{R}}^{T}_{n}\boldsymbol{x}_n \tag{5}$$

In the following sections, incremental strains in the corotational frame are based on the gradients of the incremental displacement field defined via Eq. (5).

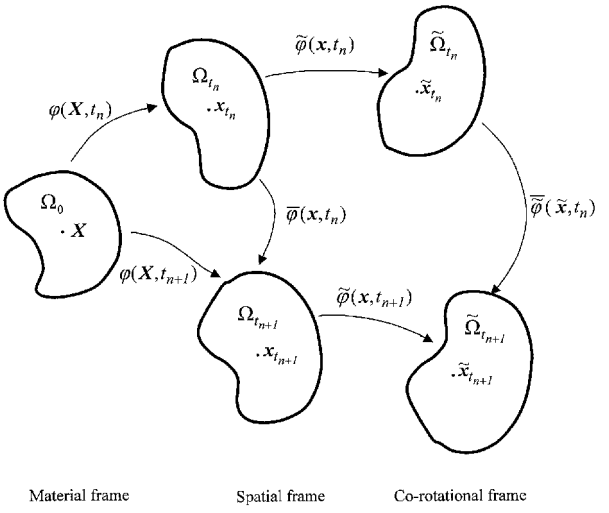

Fig. 1 Schematic diagram of material, spatial, and corotational frameworks.

III. Elasto–Plasticity in Corotational Framework

We also wish to establish the relation between $\boldsymbol{\sigma}$ and $\tilde{\boldsymbol{\sigma}}$, that is, the spatial and the rotated Cauchy stress tensors. To satisfy spatial covariance, that is, material frame indifference, the stress rate should be objective. Taking the Lie derivative of $\boldsymbol{\sigma}$ with the rotation tensor $\boldsymbol{R}$ gives rise to the well known Green–Naghdi stress rate $\boldsymbol{\sigma}^{\nabla \mathrm{GN}}$ (Refs. 8 and 16) expressed as

$$\boldsymbol{\sigma}^{\nabla \mathrm{GN}} = \boldsymbol{R}\frac{\mathrm{d}}{\mathrm{d}t}(\boldsymbol{R}^T \cdot \boldsymbol{\sigma} \cdot \boldsymbol{R}) \cdot \boldsymbol{R}^T \tag{6}$$

$$\boldsymbol{\sigma}^{\nabla \mathrm{GN}} = \boldsymbol{R} \cdot \dot{\tilde{\boldsymbol{\sigma}}} \cdot \boldsymbol{R}^T \tag{7}$$

In the elasto–plastic constitutive equations to be presented, once $\dot{\tilde{\boldsymbol{\sigma}}}$ is obtained in the rotated frame, the objective stress rate $\boldsymbol{\sigma}^{\nabla \mathrm{GN}}$ can be obtained via recourse to Eq. (7).

A. Constitutive Model

This section presents rate independent J_2 plasticity with a von Mises pressure insensitive yield condition, nonlinear isotropic and kinematic hardening rules, and an associative flow rule, all defined with respect to the rotated frame $\tilde{\Omega}_n$. However, for notational simplicity, explicit indication $(\tilde{\cdot})$ is being suppressed.

We denote the deviatoric stress and strain tensors by $\boldsymbol{s}$ and $\boldsymbol{e}$, respectively,

$$\boldsymbol{s} = \boldsymbol{\sigma} - \tfrac{1}{3}\operatorname{tr}(\boldsymbol{\sigma})\mathbf{1} \tag{8}$$

$$\boldsymbol{e} = \varepsilon - \tfrac{1}{3}\operatorname{tr}(\varepsilon)\mathbf{1} \tag{9}$$

where $\mathbf{1}$ is the second-order unit tensor and $\operatorname{tr}(\cdot)$ is the trace operator. We assume the linear spaces of deviatoric stress and deviatoric strain tensors to be equipped with the natural (Euclidean) inner product. The norms associated with these inner products are $\|\boldsymbol{s}\| = [\boldsymbol{s} : \boldsymbol{s}]^{1/2} = \sqrt{[2J_2(\boldsymbol{s})]}$ and $\|\boldsymbol{e}\| = [\boldsymbol{e} : \boldsymbol{e}]^{1/2} = \sqrt{[2J_2(\boldsymbol{e})]}$, where J_2 is the second invariant. The evolution equations for the various field variables are as follows:

1) Elastic stress:

$$\dot{\boldsymbol{\sigma}} = \boldsymbol{C}^e(\dot{\varepsilon} - \boldsymbol{d}^p) \tag{10}$$

2) Deviatoric stress:

$$\dot{\boldsymbol{s}} = 2\mu(\dot{\boldsymbol{e}} - \boldsymbol{d}^p) \tag{11}$$

3) Hydrostatic pressure:

$$\dot{p} = \tfrac{1}{3}\operatorname{tr}\dot{\boldsymbol{\sigma}} = K \operatorname{tr}\dot{\varepsilon} \tag{12}$$

4) Back stress:

$$\dot{\boldsymbol{\alpha}} = \tfrac{2}{3}\mathcal{H}'_\alpha(\bar{e}^p)\boldsymbol{d}^p \tag{13}$$

A superscript prime denotes differentiation with respect to the indicated argument, and a superposed dot indicates the derivative with respect to time. $\boldsymbol{C}^e$ is the fourth-order elastic modulus tensor defined as

$$C^{\mathrm{e}}_{ijkl} = \lambda\delta_{ij}\delta_{kl} + \mu(\delta_{ik}\delta_{jl} + \delta_{il}\delta_{jk}) \tag{14}$$

where λ and μ are Lame's parameters.

The von Mises pressure-insensitive yield condition can be expressed as

$$f(\boldsymbol{\sigma}, \boldsymbol{q}) \equiv \|\boldsymbol{\xi}\| - \sqrt{\tfrac{2}{3}}\kappa(\bar{e}^p) \leq 0 \tag{15}$$

where $\boldsymbol{q} = \{\boldsymbol{\alpha}, \bar{e}^p\}$ is a set of internal variables and $\boldsymbol{\xi}$ is defined as $\boldsymbol{\xi} = \boldsymbol{s} - \boldsymbol{\alpha}$.

The flow rule for associative plasticity that defines the plastic strain rate tensor can be written as

$$\boldsymbol{d}^p = \dot{\gamma}\frac{\partial f}{\partial \boldsymbol{\xi}} = \dot{\gamma}\hat{\boldsymbol{n}} \tag{16}$$

where $\hat{\boldsymbol{n}} = \boldsymbol{\xi}/\|\boldsymbol{\xi}\|$ is the unit normal to the yield surface and $\gamma \geq 0$ is the consistency parameter.

The evolution equation for $\bar{e}^p$ that emanates from the rate form, $\dot{\bar{e}}^p = \sqrt{(\frac{2}{3}\boldsymbol{d}^p : \boldsymbol{d}^p)}$, can be expressed as

$$\bar{e}^p = \int_0^t \sqrt{\frac{2}{3}}|\boldsymbol{d}^p(\tau)|\,\mathrm{d}\tau \tag{17}$$

The evolution equation for the yield surface can now be written as

$$\dot{\kappa} = \kappa'(\bar{e}^p)\dot{\bar{e}}^p \tag{18}$$

The Kuhn–Tucker complementary conditions that enforce consistency are

$$\dot{\gamma} \geq 0, \qquad f(\boldsymbol{\sigma}, \boldsymbol{q}) \leq 0, \qquad \dot{\gamma} f(\boldsymbol{\sigma}, \boldsymbol{q}) = 0 \tag{19}$$

Furthermore, the persistency condition can be written as

$$\dot{\gamma}\dot{f}(\boldsymbol{\sigma}, \boldsymbol{q}) = 0 \tag{20}$$

B. Constitutive Integration Scheme

From a computational standpoint the elasto–plastic problem is treated as a strain-driven problem in the sense that the stress history is obtaind from the strain history by means of an integration algorithm. An effective procedure for numerically integrating the elasto–plastic problem is to employ the so-called return mapping algorithms. For an arbitrary convex yield function, it reduces to the standard minimization problem of finding the minimum distance of a point to a convex set. In the particular case of the von Mises yield condition with associative flow rule and isotropic hardening, the closest-point projection leads to the so-called radial return algorithm.

We assume that we know the solution $(\boldsymbol{\sigma}_n, \bar{e}^p, \varepsilon_n)$ at time t_n. Our objective is to calculate the solution at time t_{n+1}, given incremental strain $\Delta\varepsilon_{n+1}$. The computational strategy is based on the operator splitting methodology and is a two-step process.

Step 1: Elastic Predictor

In the elastic predictor, inelastic flow is assumed frozen and the trial elastic stress $\boldsymbol{s}^{\mathrm{trial}}_{n+1}$ is computed from the converged values at the end of the preceding step:

$$\boldsymbol{s}^{\mathrm{trial}}_{n+1} = \boldsymbol{s}_n + 2\mu\Delta\boldsymbol{e}_{n+1} \tag{21}$$

$$\boldsymbol{\xi}^{\mathrm{trial}}_{n+1} = \boldsymbol{s}^{\mathrm{trial}}_{n+1} - \boldsymbol{\alpha}_n \tag{22}$$

At this point, yield condition (15) is checked to see whether the stress state lies in the admissible range:

$$f^{\mathrm{trial}}_{n+1} = \left\|\boldsymbol{\xi}^{\mathrm{trial}}_{n+1}\right\| - \sqrt{\tfrac{2}{3}}\kappa\left(\bar{e}^p_n\right) \leq 0 \tag{23}$$

If the state lies in the permissible range, that is, if $f^{\mathrm{trial}}_{n+1} \leq 0$, then field variables are updated by setting $(\cdot)_{n+1} = (\cdot)^{\mathrm{trial}}_{n+1}$ and the second part of the algorithm is skipped.

Step 2: Inelastic Corrector

In case the trial stress lies outside the admissible domain, it is projected onto the yield surface via enforcement of the consistency condition. Let $\hat{\boldsymbol{n}}$ denote the unit vector normal to the yield surface. For associative plasticity we have

$$\hat{\boldsymbol{n}} = \left(\left\|\frac{\partial f}{\partial \boldsymbol{\xi}}\right\|^{-1}\right)\frac{\partial f}{\partial \boldsymbol{\xi}}\bigg|_{n+1} \equiv \frac{\boldsymbol{\xi}_{n+1}}{\|\boldsymbol{\xi}_{n+1}\|}$$

In the computational setting, unit normal $\hat{\boldsymbol{n}}$ can be computed from the trial elastic stress (22) as

$$\hat{\boldsymbol{n}}_{n+1} = \boldsymbol{\xi}^{\mathrm{trial}}_{n+1} \Big/ \left\|\boldsymbol{\xi}^{\mathrm{trial}}_{n+1}\right\| \tag{24}$$

To enforce consistency at t_{n+1}, it is necessary to define the yield surface at the end of the time step and, hence, to determine the hardening parameter and back stress at t_{n+1}. The enforcement of the consistency condition (19) reduces to the scalar equation

$$g(\gamma_{n+1}) \equiv \left\|\boldsymbol{\xi}^{\mathrm{trial}}_{n+1}\right\| - \sqrt{\tfrac{2}{3}}\kappa\left(\bar{e}^p_{n+1}\right) - \left[2\mu\gamma_{n+1} + \sqrt{\tfrac{2}{3}}\left(\mathcal{H}_\alpha\left(\bar{e}^p_{n+1}\right) - \mathcal{H}_\alpha\left(\bar{e}^p_n\right)\right)\right] \equiv 0 \tag{25}$$

where $\bar{e}^p_{n+1} = \bar{e}_n + \sqrt{(\frac{2}{3})}\gamma_{n+1}$. The value of the consistency parameter γ_{n+1} can be obtained via a local Newton iteration of Eq. (25). Once γ_{n+1} is obtained, the trial stress is projected onto the yield surface via

$$\boldsymbol{s}_{n+1} = \boldsymbol{s}^{\mathrm{trial}}_{n+1} - 2\mu\gamma_{n+1}\hat{\boldsymbol{n}}_{n+1} \tag{26}$$

The equivalent plastic strain (17) is evaluated as

$$\bar{e}^p_{n+1} = \bar{e}^p_n + \sqrt{\tfrac{2}{3}}\gamma_{n+1} \tag{27}$$

With the aid of Eq. (27), the evolution equation (13) can now be integrated to obtain

$$\boldsymbol{\alpha}_{n+1} = \boldsymbol{\alpha}_n + \sqrt{\tfrac{2}{3}}\Delta\mathcal{H}_\alpha\hat{\boldsymbol{n}}_{n+1} \tag{28}$$

where $\Delta\mathcal{H}_\alpha \equiv \mathcal{H}_\alpha(\bar{e}^p_{n+1}) - \mathcal{H}_\alpha(\bar{e}^p_n)$. From Eqs. (26) and (28) we obtain

$$\boldsymbol{\xi}_{n+1} \equiv \boldsymbol{s}_{n+1} - \boldsymbol{\alpha}_{n+1} = \boldsymbol{\xi}^{\text{trial}}_{n+1} - \left[2\mu\gamma_{n+1} + \sqrt{\tfrac{2}{3}}\Delta\mathcal{H}_\alpha\right]\hat{\boldsymbol{n}}_{n+1} \tag{29}$$

The updated Cauchy stress in the corotational frame is obtained via adding the hydrostatic pressure:

$$\boldsymbol{\sigma}_{n+1} = K\,\text{tr}[\Delta\boldsymbol{\varepsilon}_{n+1}]\mathbf{1} + \boldsymbol{s}_{n+1} \tag{30}$$

Remark: Note that Eq. (30) is defined in the rotated configuration $\tilde{\Omega}^{(i)}_{n+1}$. For notational simplicity we have dropped explicit indication of the superposed tilde ($\tilde{\cdot}$) in all of the equations presented in Sec. III.A. The Green–Naghdi stress rate $\boldsymbol{\sigma}^{\nabla\text{GN}}$ is obtained via recourse to Eq. (7).

IV. Variational Problem

A well-defined boundary-value problem requires consideration of the equilibrium equations and a set of suitable boundary conditions in addition to the constitutive relations. As mentioned in Sec. II, $\Omega_0 \subset R^{n_{\text{sd}}}$ is an open set with piecewise smooth boundary Γ_0 at time t_0. We assume that Γ_0 admits the following decomposition:

$$\Gamma_{g0} \cup \Gamma_{h0} = \Gamma_0 \tag{31}$$

$$\Gamma_{g0} \cap \Gamma_{h0} = \varnothing \tag{32}$$

where Γ_{g0} and Γ_{h0} are open sets in Γ_0 and represent the portions of boundary with prescribed essential and natural boundary conditions, respectively.

The space of admissible configurations is defined as

$$\mathcal{S} = \left\{\varphi\colon \Omega_0 \to R^{n_{\text{sd}}} \mid \det[D\varphi] > 0 \text{ in } \Omega \text{ and } \varphi|_{\Gamma_{g0}} = \hat{\varphi}\right\}$$

where $\hat{\varphi}$ is assumed prescribed on the Dirichlet boundary. The space of admissible variations $\mathcal{V}$ is defined as

$$\mathcal{V} = \left\{\eta_0\colon \Omega_0 \to R^{n_{\text{sd}}} \mid \eta_0|_{\Gamma_{g0}} = 0\right\} \tag{33}$$

We can write the formal statement of the weak form in the current configuration as follows: Find $\varphi_t \in \mathcal{S}$ such that $\mathcal{G}(\varphi_t, \eta) = 0$ for all $\eta \in \mathcal{V}$:

$$\mathcal{G}(\varphi_t, \eta) = \int_{\Omega_t} [\boldsymbol{\sigma}\colon (\nabla\eta \circ \varphi_t)]\,d\Omega - \int_{\Omega_t} \rho\boldsymbol{b}\cdot(\eta\circ\varphi_t)\,d\Omega - \int_{\Gamma_{h_t}} \boldsymbol{t}\cdot(\eta\circ\varphi_t)\,d\Gamma \tag{34}$$

where $\boldsymbol{t}$ is the traction vector specified on the part $\Gamma_{h_t} = \varphi_t(\Gamma_h)$ of the boundary.

The numerical solution of the weak form of nonlinear problems is accomplished via iterative schemes that are based on the solution of a sequence of linearized problems. We consider a process of incremental loading whereby the deformation mapping over Ω_0 changes from φ_{t_n}, at time t_n, to $\varphi_{t_{n+1}} = \varphi_{t_n} + \boldsymbol{u}$, at time $t_{n+1} = t_n + \Delta t$. Equilibrium is then enforced weakly at time t_{n+1} via the variational or weak form of the problem. The corresponding incremental problem is obtained by linearizing the weak form about a sequence of configurations and can typically be written as

$$\begin{aligned}\text{D}\mathcal{G}\left(\varphi^{(i)}_{n+1}, \eta\right)\cdot\boldsymbol{u}^{(i)}_{n+1} &\equiv \int_{\Omega_t}\left[\frac{1}{J}\,\text{tr}\left(\nabla\eta\boldsymbol{\tau}^{(i)}_{n+1}\nabla\boldsymbol{u}^{(i)}_{n+1}\right) + \nabla\eta\colon\left(\boldsymbol{c}^{(i)}_{n+1}\colon\nabla\boldsymbol{u}^{(i)}_{n+1}\right)\right]d\Omega \\ &= -\mathcal{G}\left(\varphi^{(i)}_{n+1}, \eta\right)\end{aligned} \tag{35}$$

Iteration is continued until the residual $\mathcal{G}(\varphi^{(i)}_{n+1}, \eta)$ vanishes to within a prescribed tolerance. Also, $\boldsymbol{c}^{(i)}_{n+1}$ represents the tangent modului consistent with the radial return algorithm as derived in Sec. IV.A (see Simo and Taylor[17]).

A. Continuum-Based Composite Shell Element

The constitutive model is implemented in a continuum-based eight-node hexahedral corotational element that is specially designed to model the bending-dominated response in multilayered shells.[7] Displacements and rotations are assumed finite, whereas incremental strains are infinitesimal. The element is free of volumetric and shear locking and possesses very good coarse mesh accuracy. By modeling each material layer through the composite thickness via a layer of these elements together with the corresponding elasto–plastic constitutive equations, we accommodate the elasto–plastic response of individual material layers in the laminate. These individual material matrices are mapped onto the corotational frame to perform consistent numerical integration of the element level quantities (for details, see Masud et al.[7]).

B. Consistent Tangent Operator

We now present the tangent moduli $\boldsymbol{c}_{n+1}$ that is consistent with the radial return algorithm. The explicit form of the incremental response function $\bar{\boldsymbol{\sigma}}(\boldsymbol{\sigma}_n, \boldsymbol{\varepsilon}_n, \bar{e}^p_n, \boldsymbol{\varepsilon} - \boldsymbol{\varepsilon}_n)$ can be written as

$$\bar{\boldsymbol{\sigma}}\left(\boldsymbol{\sigma}_n, \boldsymbol{\varepsilon}_n, \bar{e}^p_n, \boldsymbol{\varepsilon} - \boldsymbol{\varepsilon}_n\right) \equiv K\,\text{tr}(\Delta\boldsymbol{\varepsilon}_{n+1})\mathbf{1} + \boldsymbol{\alpha}_{n+1} + R_{n+1}\hat{\boldsymbol{n}} \tag{36}$$

where $R_{n+1} \equiv \sqrt{(\frac{2}{3})}\kappa(\bar{e}^p_{n+1})$ is the radius of the yield surface at $t = t_{n+1}$. Following Simo and Taylor,[17] the tangent moduli $\boldsymbol{c}_{n+1}$ is then defined as

$$\boldsymbol{c}_{n+1} = \left.\frac{\partial\bar{\boldsymbol{\sigma}}\left(\boldsymbol{\sigma}_n, \boldsymbol{\varepsilon}_n, \bar{e}^p_n, \boldsymbol{\varepsilon} - \boldsymbol{\varepsilon}_n\right)}{\partial\boldsymbol{\varepsilon}}\right|_{\boldsymbol{\varepsilon} = \boldsymbol{\varepsilon}_{n+1}} \tag{37}$$

Substituting Eq. (36) in Eq. (37) and applying the chain rule, we obtain the following expression for $\boldsymbol{c}_{n+1}$:

$$\begin{aligned}\boldsymbol{c}_{n+1} = K\mathbf{1}\otimes\mathbf{1} + 2\mu\frac{R_{n+1}}{\left\|\boldsymbol{\xi}^{\text{trial}}_{n+1}\right\|}\left[\boldsymbol{I} - \frac{1}{3}\mathbf{1}\otimes\mathbf{1}\right] - 2\mu\frac{R_{n+1}}{\left\|\boldsymbol{\xi}^{\text{trial}}_{n+1}\right\|}\hat{\boldsymbol{n}}\otimes\hat{\boldsymbol{n}} \\ + \hat{\boldsymbol{n}}\otimes\frac{\partial R_{n+1}}{\partial\boldsymbol{\varepsilon}_{n+1}} + \frac{\partial\boldsymbol{\alpha}_{n+1}}{\partial\boldsymbol{\varepsilon}_{n+1}}\end{aligned} \tag{38}$$

After some calculations, the final expression for the tangent moduli consistent with radial return algorithm for nonlinear isotropic/kinematic hardening is obtained as

$$\boldsymbol{c}_{n+1} = K\mathbf{1}\otimes\mathbf{1} + 2\mu\beta\left[\boldsymbol{I} - \tfrac{1}{3}\mathbf{1}\otimes\mathbf{1}\right] - 2\mu\chi\hat{\boldsymbol{n}}\otimes\hat{\boldsymbol{n}} \tag{39}$$

where β and χ are given by

$$\beta = \sqrt{\frac{2}{3}}\frac{\kappa_{n+1} + \Delta H_\alpha}{\left\|\boldsymbol{\xi}^{\text{trial}}_{n+1}\right\|}$$

$$\chi = 1\Big/\left\{1 + \frac{[\kappa' + H'_\alpha]_{n+1}}{3\mu}\right\} - (1-\beta) \tag{40}$$

Remark: All quantities presented here are defined in the rotated configuration $\tilde{\Omega}^{(i)}_{n+1}$.

V. Numerical Examples

We now present elasto–plastic response of multilayered plates and shells to validate the framework and to show its range of application.

A. Necking of a Circular Rod

The first numerical simulation is necking of a circular rod under displacement control (Figs. 2a and 2b). This problem has been selected from Simo,[10] wherein the author has employed a hyperelastic–plastic model. The radius of the rod is 6.413 mm, and its length is 53.334 mm. Material properties of the rod are shown in Table 1. The computational mesh is composed of 400 corotational hexahedral elements.[7] Total load is applied in 200 equal load steps. Necking is initiated by providing a 2% reduction in the cross-sectional area. Nonlinear hardening function $\kappa(\bar{e}^p)$ is defined as

$$\kappa(\bar{e}^p) = \sigma_0 + (\sigma_\infty - \sigma_0)[1 - \exp(-\delta\bar{e}^p)] \tag{41}$$

Table 1 Material properties for the circular rod

Quantity	Value
Shear modulus μ	80.1938 GPa
Bulk modulus K	164.206 GPa
Initial flow stress σ_0	0.45 GPa
Residual flow stress σ_∞	0.715 GPa
Saturation exponent δ	16.93

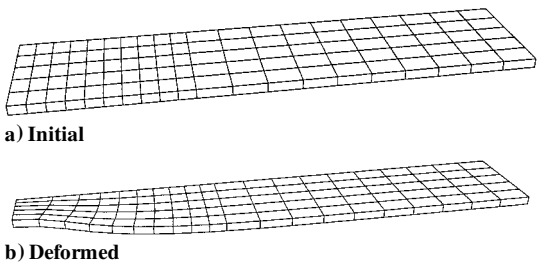

Fig. 2 Mesh.

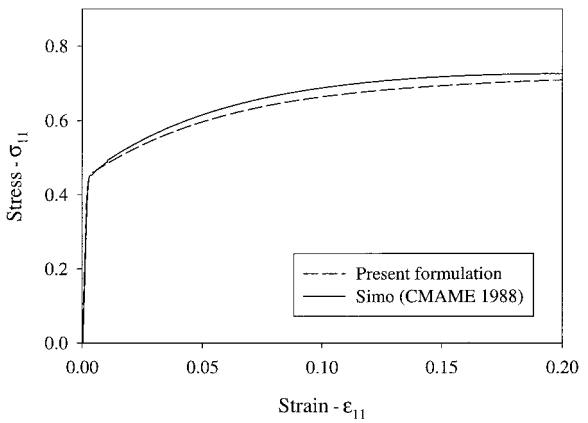

Fig. 3a Stress–strain plot in hypoelastic and hyperelastic frameworks.

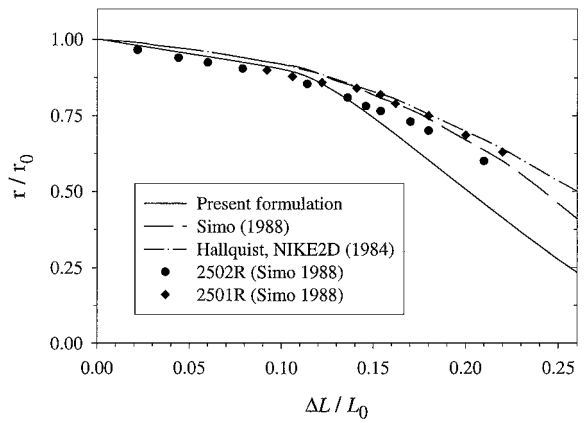

Fig. 3b Normalized neck vs normalized elongation.

where σ_0 is the initial flow stress and σ_∞ is the residual flow stress. Figure 3a presents the stress–strain response for the given material properties. We have compared the present hypoelastic model cast in the corotational framework with the finite deformation hyperelastic model by Simo.[10] For small to medium range in strains that develop in this problem, the present formulation shows a stable response in the stress–strain behavior. Figure 3b presents the evolution of neck vs axial elongation of the rod and shows a good comparison with Simo[10] and Hallquist[18] for up to 15% engineering strains.

B. Elasto–Plastic Cantilever Plate Under Tip Load

This simulation presents elasto–plastic response of a thin cantilever plate subjected to a concentrated load at the tip. Figure 4 shows the initial and the final deformed geometry of the plate. Material and geometric properties of the plate are shown in Table 2. The mesh is composed of $10 \times 1 \times 2$ elements. Two simulations were done wherein the total load was applied in 10 steps and 20 steps, respectively. Applied load vs deflection for the load point (Fig. 5) shows a close agreement with Dvorkin et al.[19] wherein the authors have employed a multiplicative finite strain framework together with hyperelastic constitutive equations. Figure 6 shows a study of the sensitivity of the response with respect to the mesh refinement wherein the load is applied in 20 equal steps. A difference of about 5% is observed which is within the permissible limits of spatial accuracy for such problems.

Table 2 Material properties and geometric data for the narrow cantilever plate

Quantity	Value
Young's modulus E	1.2×10^7 kN/m^2
Plastic tangent modulus E_t	1.2×10^5 kN/m^2
Yield stress σ_y	2.4×10^4 kN/m^2
Poisson's ratio ν	0.3
Length L	10.0 m
Width B	1.0 m
Thickness t	0.1 m

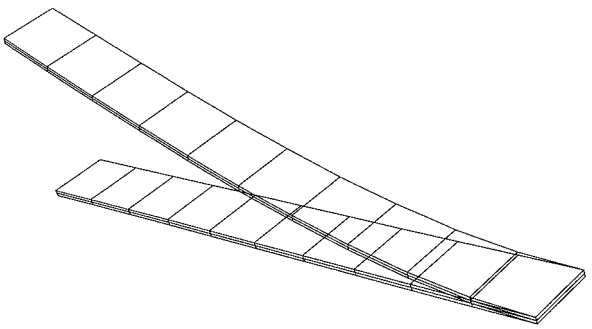

Fig. 4 Initial and deformed mesh of the beam.

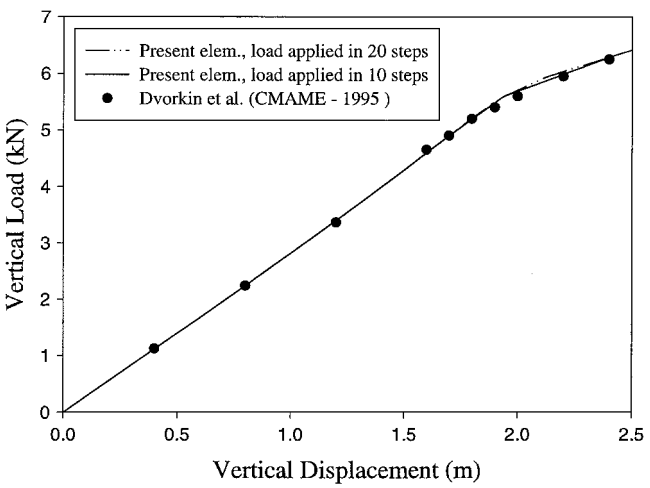

Fig. 5 Load-deflection diagram at load point of the elasto–plastic beam.

C. Elasto–Plastic Cylindrical Shell with Free Edges

We now present elasto–plastic analysis of a cylindrical shell with free edges, subjected to two opposite point loads (Fig. 7). The shell is able to undergo finite rotations, and, therefore, this problem provides a severe test for the veracity of the underlying formulation. Material and geometeric properties of the shell are shown in Table 3. The cylinder possesses two layers through its thickness. Invoking symmetry, only one-eighth of the shell is modeled using $16 \times 8 \times 2$ elements (16 along the periphery, 8 along the length, and 2 through the thickness). The second refined mesh contains $24 \times 8 \times 2$ elements. The total load is applied in 140 equal load steps.

Table 3 Material properties and geometric data for the cylindrical shell

Quantity	Value
Young's modulus E	10.5×10^3 kN/m^2
Plastic tangent modulus E_t	10.5×10^2 kN/m^2
Yield stress σ_y	1.05×10^2 kN/m^2
Poisson's ratio ν	0.3125
Length L	10.35 m
Radius R	4.953 m
Thickness t	0.094 m

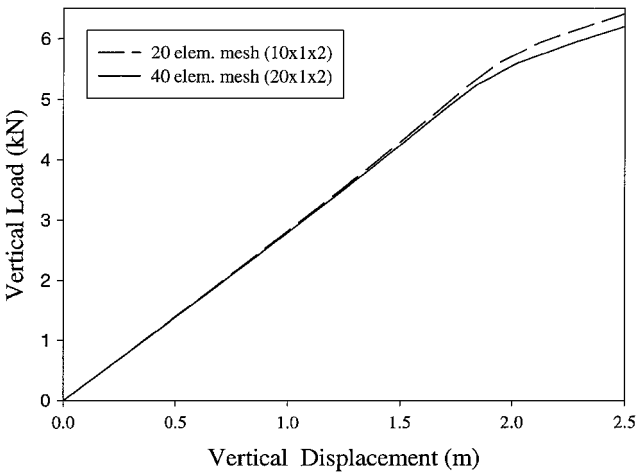

Fig. 6 Mesh refinement of elasto–plastic cantilever beam.

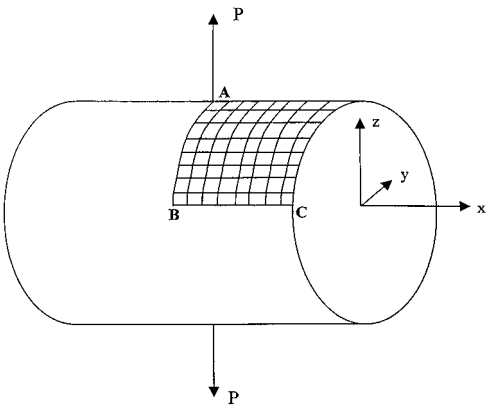

Fig. 7 Schematic diagram of the problem.

The initial and the final deformed configuration of the shell is shown in Figs. 8a and 8b. Figure 9 shows the load-deflection diagram at 1) point A, which is a point directly under the load, 2) point B, which is a point on the side of the shell and undergoes horizontal displacement, and 3) point C, which is a point on the free edge at the side of the shell. We first present comparison with Jiang and Chernuka,[20] considering the material to be elastic in the entire range of deformation. We then consider the material to undergo elasto–plastic deformation, where the plastic tangent modulus is taken to be 10% that of the elastic tangent modulus. We observe that the cylindrical shell buckles plastically and that the buckling load is much lower than the value obtained if the material were considered elastic in the entire range of deformation. Once again the difference in the numerical results for the two meshes is less than 4%.

D. Elasto–Plastic Hemispherical Shell

We now present the elasto–plastic response of a hemispherical shell composed of two layers through the thickness. The undeformed configuration of the shell has a 18-deg hole at the top and is subjected to two inward and two outward forces that are 90 deg apart. Material and geometeric properties of the spherical shell are given in Table 4. Because of symmetry, only one quadrant needs to be modeled. Two meshes are used in this study. First mesh is composed of $16 \times 16 \times 2$ elements, and the second mesh is composed of $18 \times 18 \times 2$ elements. Total load is applied in 100 equal steps.

Figure 10 shows the final deformed configuration of the mesh without any magnification of deformation. A plot of pinching loads

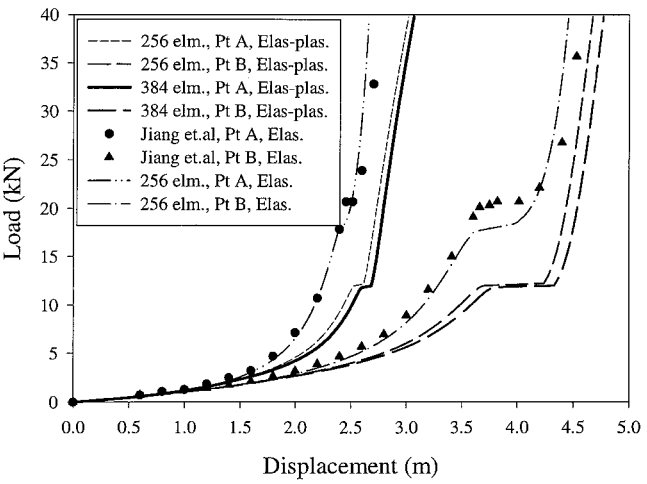

Fig. 9 Load-deflection diagram for cylindrical shell.

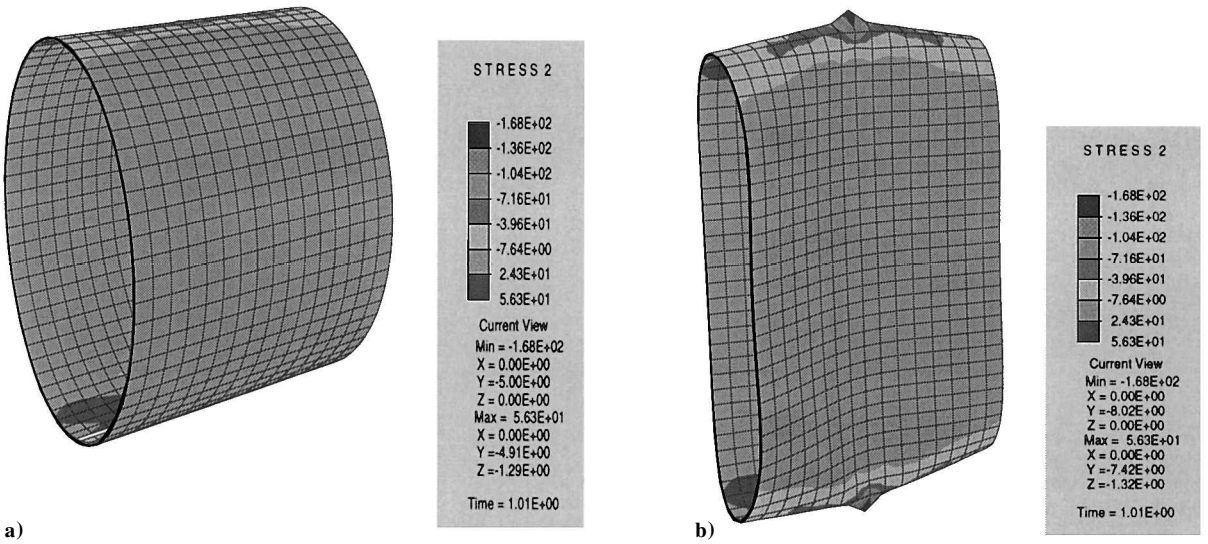

Fig. 8 Initial and final deformed geometry with stress σ_{xy}.

vs deflections under the corresponding loads is shown in Fig. 11. In the absense of elasto–plastic response reported in the literature for this problem, we provide a qualitative comparison with Simo et al.,[21] wherein the material is assumed to be linear elastic in the entire range of deformation. Although the elasto–plastic response is softer than the pure elastic response, strains still stay in the moderate regime and close to the elastic strian range even for this extremely large deformation. This comparison shows that the present problem is dominated by large rotations and not by large strains.

E. Elasto–Plastic Analysis of a Composite Cylindrical Shell

The last numerical simulation is elasto–plastic analysis of a composite cylindrical shell with free edges, subjected to two opposite point loads as shown in Fig. 7. The cylinder is composed of two layers through its thickness; the outer layer is aluminum and the inner layer is copper. These layers are assumed to be perfectly bonded at the common interface throughout the entire range of deformation. Material and geometric properties of the composite shell are shown in Table 5. Invoking symmetry, only one-eighth of the shell is modeled. Figure 12 shows the load-deflection diagram for two different mesh configurations. The first mesh contains $24 \times 8 \times 2$ elements, whereas the second mesh contains $16 \times 16 \times 2$ elements. In either case, the total load is applied in 200 equal load steps.

The overall response represents two distinct features: an initial portion, which is dominated by bending and is characterized by large displacement and rotation, and a later portion, which is dominated by membrane effects that are characterized by a stiff behavior. The difference in the numerical results for the two meshes is less than 4%, which is well within the permissible limits of spatial accuracy for this type of problems.[22]

Table 4 Material properties and geometric data for the hemispherical shell

Quantity	Value
Young's modulus E	6.825×10^7 psi
Plastic tangent modulus E_t	6.825×10^6 psi
Yield stress σ_y	6.825×10^5 psi
Poisson's ratio ν	0.3
Radius R	10 in.
Thickness t	0.04 in.

Table 5 Material properties and geometric data for composite cylindrical shell

Quantity	Aluminum	Copper
Young's modulus E, kN/m^2	10.0×10^3	18.0×10^3
Plastic tangent modulus E_t, kN/m^2	10.0×10^2	18.0×10^2
Yield stress σ_y, kN/m^2	0.4×10^2	1.1×10^2
Poisson's ratio ν	0.33	0.33
Length L, m	10.35	10.35
Radius R, m	4.9763	4.5695
Thickness t, m	0.047	0.047

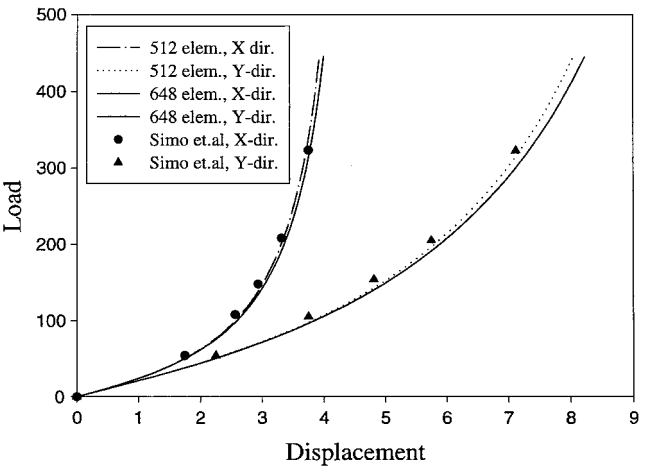

Fig. 11 Load-deflection diagram of the elasto–plastic pinched hemispherical shell.

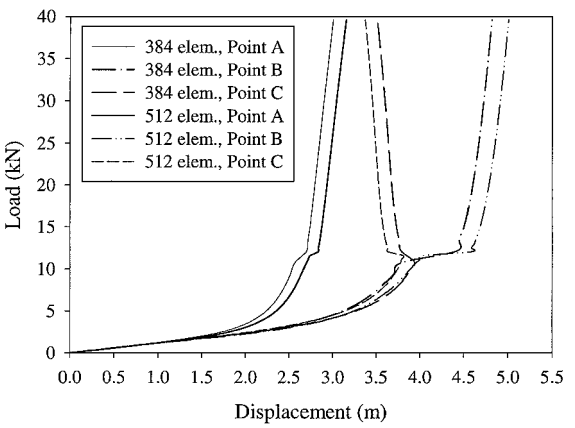

Fig. 12 Load-deflection diagram for hemispherical shell.

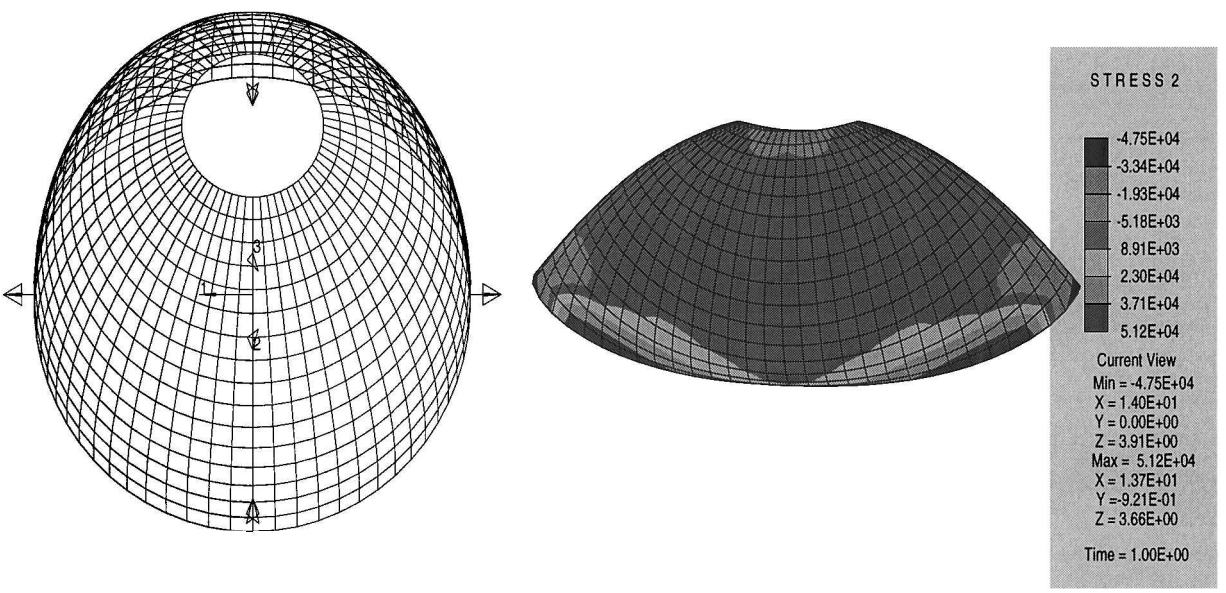

Fig. 10 Initial and final deformed geometry and stress σ_{xy}.

VI. Conclusions

We have presented a continuum-based corotational framework for modeling large deformation elasto–plastic response in multilayered composites. Accordingly, we have cast the elasto–plastic constitutive equations in the corotational frame as well. An advantage of the corotational formulation is that frame invariance requirements do not limit constitutive equations to isotropic elastic response, which is an important issue in modeling composites. Furthermore, the proposed corotational procedure provides a general framework that allows the incorporation of small strain constitutive models, which are relatively easy to develop, for finite deformation analysis. This is a specially attractive feature for the modeling of composites wherein the existence of material anisotropy and a wide range in inherent material length scales render the development of a finite strain constitutive model an exceedingly difficult task. The proposed framework is conceptually simple and computationally economic as compared to finite strain elasto–plastic frameworks that would otherwise be required to solve the class of problems presented here. Furthermore, from a practical viewpoint, the presence of reinforcing fibers in advanced laminated composites typically used in the aerospace, marine, and automotive industries restrict the strains to lie in the small to moderate range. Accordingly, from a kinematic standpoint, an issue of significance in large deformation analysis of composite plates and shells made of these engineered materials is that of finite rotations, which is very effectively handled in the corotational framework. Numerical simulations show the good accuracy and stability properties of the proposed model and the range of applicability of the proposed framework.

Acknowledgments

This research was supported by the National Science Foundation Under Grants CMS-9812205 and 9813386.

References

[1]Putcha, N. S., and Reddy, J. N., "A Refined Mixed Shear Flexible Finite Element for the Nonlinear Analysis of Laminated Plates," *Computers and Structures*, Vol. 22, No. 4, 1986, pp. 529–538.

[2]Liao, C. L., and Reddy, J. N., "Analysis of Anisotropic, Stiffened Composite Laminates Using a Continuum-Based Shell Element," *Computers and Structures*, Vol. 34, No. 6, 1990, pp. 805–815.

[3]Yang, H. T. Y., Saigal, S., Masud, A., and Kapania, R. K., "A Survey of Recent Shell Finite Elements," *International Journal for Numerical Methods in Engineering,* Vol. 47, 2000, pp. 101–127.

[4]Reddy, J. N., *Mechanics of Laminated Composite Plates: Theory and Analysis*, CRC Press, Boca Raton, FL, 1996.

[5]Masud, A., and Panahandeh, M., "A Finite Element Formulation for the Analysis of Laminated Composites," *Journal of Engineering Mechanics*, Vol. 125, No. 10, 1999, pp. 1115–1124.

[6]Masud, A., and Tham, C. L., "A Finite Element Model for Geometrically Nonlinear Analysis of Multi-Layered Composite Shells," *Computational Mechanics in Structural Engineering*, edited by F. Y. Cheng and Y. X. Gu, Elsevier Science, NewYork, 1999.

[7]Masud, A., Tham, C. L., and Liu, W. K., "A 3-D Co-Rotational Formulation for Geometrically Nonlinear Analysis of Multi-Layered Composite Shells," *Computational Mechanics*, Vol. 26, No. 1, 2000, pp. 1–12.

[8]Simo, J. C., and Hughes, T. J. R., *Computational Inelasticity*, Springer-Verlag, New York, 1998.

[9]Simo, J. C., "A Framework for Finite Strain Elasto-Plasticity Based on Maximum Plastic Dissipation and Multiplicative Decomposition: Part I. Continuum Formulation," *Computational Methods in Applied Mechanical Engineering*, Vol. 66, 1988, pp. 199–219.

[10]Simo, J. C., "A Framework for Finite Strain Elasto-Plasticity Based on Maximum Plastic Dissipation and Multiplicative Decomposition: Part II. Computational aspects," *Computational Methods in Applied Mechanical Engineering*, Vol. 68, 1988, pp. 1–31.

[11]Simo, J. C., and Marsden, J. E., "On the Rotated Stress Tensor and the Material Version of the Doyle–Ericksen Formula," *Archives of Rational Mechanics and Analysis*, Vol. 86, 1984, pp. 213–231.

[12]Atluri, S. N., and Cazzani, A., "Rotations in Computational Solid Mechanics," *Archives for Computational Methods in Engineering*, Vol. 2, 1994, pp. 49–138.

[13]Moita, G. F., and Crisfield, M. A., "A finite Element Formulation for 3-D Continua Using the Co-Rotational Technique," *International Journal for Numerical Methods in Engineering,* Vol. 39, 1996, pp. 3775–3792.

[14]Rankin, C. C., and Brogan, F. A., "An Element Independent Co-Rotational Procedure for the Treatment of Large Rotations," *Journal of Pressure Vessel and Technology*, Vol. 108, 1986, pp. 165–174.

[15]Belytschko, T., and Hsieh, B. J., "Non-Linear Transient Finite Element Analysis with Convected Coordinates," *International Journal for Numerical Methods in Engineering,* Vol. 7, 1973, pp. 255–271.

[16]Marsden, J. E., Hughes, T. J. R., *Mathematical Foundations of Elasticity*, Dover, New York, 1994.

[17]Simo, J. C., and Taylor, R. L., "Consistent Tangent Operators for Rate Independent Elasto-Plasticity," *Computational Methods in Applied Mechanical Engineering*, Vol. 48, 1985, pp. 101–118.

[18]Hallquist, J. O., "NIKE 2D: An Implicit, Finite Deformation, Finite Element Code for Analyzing the Static and Dynamic Response of Two-Dimensional Solids," Lawrence Livermore National Lab., Rept. UCRL-52678, Univ. of California, Livermore, CA, 1984.

[19]Dvorkin, E. N., Pantuso, D., and Repetto, E. A., "A Formulation of the MITC4 Shell Element for Finite Strain Elasto-Plastic Analysis," *Computational Methods in Applied Mechanical Engineering*, Vol. 125, 1995, pp. 17–40.

[20]Jiang, L., and Chernuka, M. W., "A Simple Four-Noded Co-Rotational Shell Element for Arbitrarily Large Rotations," *Computers and Structures*, Vol. 53, 1994, pp. 1123–1132.

[21]Simo, J. C., Fox, D. D., and Rifai, M. S., "On a Stress Resultant Geometrically Exact Shell Model, Part III: Computational Aspects of the Nonlinear Theory," *Computational Methods in Applied Mechanical Engineering*, Vol. 79, 1990, pp. 21–70.

[22]Liu, W. K., Guo, Y., Tang, S., and Belytschko, T., "A Multiple-Quadrature Eight-Node Hexahedral Finite Element for Large Deformation Elasto-Plastic Analysis," *Computational Methods in Applied Mechanical Engineering*, Vol. 154, 1998, pp. 69–132.

S. Saigal
Associate Editor